Interference analysis for optical wireless communications in Network-on-Chip (NoC) scenarios

Jinous Shafiei Dehkordi and Velio Tralli

Abstract—**Optical wireless (OW) communications, besides being of great interest for indoor and outdoor applications, have been recently proposed as a powerful alternative to the existing wired and wireless radio frequency (RF) interconnects in network-on-chips (NoCs). Design and analysis of networks with OW links require a careful investigation of cross-link interference, which impacts considerably the efficiency of systems that reuse the same channel for multiple transmissions. Yet, there is no comprehensive analysis of interference for OW NoCs, and the analyses of crosstalk in optical waveguide communications usually rely on synchronous data transmissions. A novel framework for the analysis of on-chip OW communications in the presence of cross-link cochannel interference and noise is proposed, where asynchronous data transmissions are considered. Self-beating of interfering signals is also considered, which was often neglected in previous literature. The bit error probability (BEP) for arbitrary number of interfering sources is derived as a function of signal-to-noise ratio (SNR), interference powers, detection threshold and pulse shaping, using both exact and approximation methods. The proposed analysis can be applied to both noise- and interference-limited cases, and enables a system designer to evaluate reuse distance between links that share the same optical carrier for simultaneous communication in NoCs.**

I. INTRODUCTION

Optical wireless (OW) communications are among the promising solutions to growing bandwidth demand in macro-scale networks for a vast range of indoor and outdoor applications [1]–[3]. In micro-scale networks, OW links have been recently proposed as an interconnect technology [4]–[6] to provide efficient communication in network-on-chips (NoCs) [7]. The continuous increase in the density of processing cores cannot rely only on the traditional metal interconnections, since they have intrinsic limitations in communication bandwidth and power consumption [8]–[10]. These limitations have inspired many researchers to look for alternative technologies, like optical wired interconnects using silicon photonics [11]–[13] and wireless interconnects using radio frequency (RF) [14]–[20].

Optical NoCs exploit the optical domain to provide high bandwidth, low power consumption, low latency and fast

signal propagation [21]. However, there are several issues for the design of NoCs using optical wired interconnects [13], [22]. The electrical-optical conversions at cores increase signal propagation delay and power consumption [13]. In such networks, as the number of cores scales up, the complexity of switching and routing increases occupying chip area, and the power losses due to multiple waveguide crossings become significant. Wireless interconnects can replace long distance connections in a hybrid architecture, thus simplifying network topology and routing issues [16]–[19], [23], [24]. In [25], multi-hop wired paths are replaced with single-hop wireless links to overcome high power consumption and routing problems. Wireless interconnects also improve broadcast efficiency in large-scale chip multiprocessors [26]–[28]. However, on-chip RF communication is outperformed by optical technology in terms of available bandwidth and integrability [4], whereas wireless NoCs have been investigated only in millimeter-wave and sub-teraherz bands [29], [30]. Moreover, the utilization of RF interconnects in NoCs may cause near-field coupling, thus degrading the communication performance [31]. These limitations motivate research into higher frequency bands for on-chip wireless communications.

OW technologies have been recently proposed to take advantage of both wireless and optical technologies, where wireless interconnects are improved with high bandwidth, far-field propagation and easier antenna integration compared to RF links [4]. The same wavelength propagating on optical waveguides can be used by wireless links without electrical-optical conversion [5]. The design of on-chip antennas at optical frequencies and suitably coupled with silicon waveguides is recently underway [5] after an earlier work in [26]. The first contributions on channel modeling by using electromagnetic simulation and ray-tracing have been presented in [4], [6]. However, the performance and feasible design of on-chip OW links have not yet been addressed, and their application needs further investigation. Design and analysis of networks with wireless links require a careful study of cross-link interference, which occurs between links that reuse the same frequency channel. The frequency (wavelength) reuse in communications increases the network capacity, but, on the other hand, causes cochannel interference degrading system performance. Hence, for the design of wireless NoCs, there is a trade-off between the spectrum usage efficiency and communication performance.

In optical communications with narrow-linewidth laser sources, the beating between desired and interfering signals

creates crosstalk at the photodetector (PD) [32]. In [33]–[38], the crosstalk in networks with synchronous data transmissions was analyzed for noise-limited systems, but in OW networks subject to heavy interference, the link performance is limited by both noise and interference. Yet, the impact of interference on OW communications in NoCs has not been explored. Moreover, data sources in NoCs may be asynchronous, which is in contrast with much published works. In [39], the bit error probability (BEP) was provided for indoor infrared wireless communications, where an asynchronous interference-limited system is considered. In such networks with large linewidth optical sources (e.g., light-emitting diode (LED)), the beating contributions become negligible, thus simplifying interference analysis, which cannot be applied to OW NoCs with narrow linewidth laser sources. Recall that the reliability is an essential requirement for communication systems, which is often measured in terms of BEP. In the literature on OW NoCs, there is no analysis for the BEP or other communication performance metrics. By establishing an interference-aware framework, a network designer can find the optimal configuration that meets the required reliability for on-chip communication. For example, one can investigate how many links using the same wavelength can operate in the NoC and which distance should separate them, such that the required level of reliability is satisfied.

This paper analyzes cochannel interference in NoCs with OW links operating at the same wavelength. Unlike previous published works, asynchronous data transmissions with intensity modulation and direct detection are considered. By extending the analytical methods in [37], [40], the BEP is derived based on both exact and approximation approaches, and the accuracy of tight approximations is verified for different network settings. The proposed analysis considers narrow-linewidth lasers, but it can also be applied to the cases of large-linewidth optical sources in micro- and macro-scale OW scenarios [41]. The self-beating of interfering signals is also considered in the analysis, and a comparison between the cases with and without self-beating contributions is provided. In a case of study, we investigate how to design the distances among all transmit and receive antennas to preserve a required BEP, while sharing the same frequency channel by multiple OW links. The novel contributions of the paper to the existing literature are summarized as follows:

- investigation of OW link performance for the NoC scenarios in the presence of cochannel interference due to the optical carrier sharing;
- analytical evaluation of the BEP as a function of signal-to-noise ratio (SNR), interfering powers, number of interfering sources, detection threshold and pulse shaping, considering asynchronous data transmission and self-beating of interfering signals;
- application of the analysis to both noise- and interference-limited systems and evaluation of the reuse distance among simultaneously transmitting links.

The rest of the paper is organized as follows. Section II describes the NoC scenario and Section III presents the link model. Section IV provides exact and approximate expressions
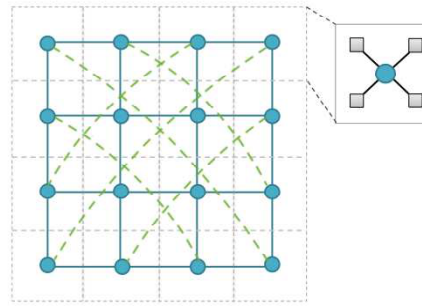

Figure 1. An example of hybrid wired-wireless NoC topology. Dashed and solid lines among circles (hubs/routers) are wireless and wired links, respectively, small rectangles show cores.

for the BEP based on two types of decision thresholds, namely, average optical power (AOP) and middle of the eye (MoE). Numerical results are illustrated in Section V showing the accuracy of the derived expressions for the BEP, and system sensitivity to the network parameters; it is also shown how to apply the proposed tools for evaluating the reuse distance of OW links in NoCs. Finally, conclusions follow in Section VI.

Notations: Throughout the paper, $\mathbb{E}\{\cdot\}$ denotes statistical expectation; vectors are indicated with bold symbols, and $\sim$ denotes *distribution*.

II. NoC scenario with OW interconnects

Consider a NoC, which utilizes both wired and wireless interconnects to provide communication among cores. The architectures of hybrid NoCs can be generally classified as mesh topology based and small-world networks based [25]. In mesh topology based NoCs, a two-tier design is considered, where the first tier is a base network with 2D regular mesh topology that provides short wired links between nodes, and the second tier provides long-range connections through wireless links [17], [23]. In small-world networks based NoCs, wired links connect neighboring nodes, and wireless links connect some distant or high traffic nodes according to the placement schemes [14], [29]. In this work, we consider a hybrid NoC architecture, where a locally connected wired network is overlaid by OW links as shown in Fig. 1. In such NoC, each network node is a router/hub serving a cluster of cores, which are connected through wired links.

The physical structure of on-chip interconnects can be represented by a layered model [6]. The first layer is the silicon substrate, which includes all electronic components. The second layer made of several metals and dielectric tiers provides the interconnections for circuits and devices inside the cores, as well as wired interconnections for cores, routers and other NoC elements. The optical layer is located at the top of these two layers, where a suitable interface between the optical and electrical layers is applied [13]. The optical layer incorporates the photonic components, like PDs, optical waveguide links and optical nanoantennas. In this layer, optical signals are transmitted through silicon waveguides and wireless links. The
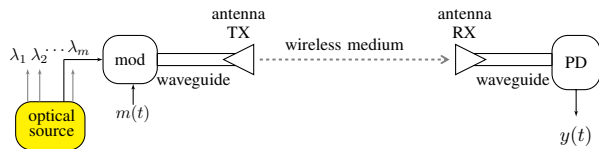
Figure 2. OW link model.

optical nanoantennas [6] are coupled with silicon waveguides and radiate the optical signals in a wireless transmission medium, made of silicon dioxide or other similar dielectric materials. The gain of the antenna is denoted by G, which is closely related to the antenna directivity. Recall that increasing the antennas directivity reduces link power losses, while decreasing the antenna directivity provides the wide beamwidth required for broadcast communication [5]. A laser source (off-chip) provides the optical power by emitting unmodulated light at multiple wavelengths $\{\lambda_1, \lambda_2, \ldots, \lambda_m\}$, which are coupled to the waveguides in the optical layer [13]. In an OW link, the optical carrier is modulated by the digital signal $m(t)$ and passed through waveguides to the transmit nanoantenna (see Fig. 2). The optical signal propagates into a wireless medium (dashed line) and is received by a nanoantenna again coupled to the optical waveguide. The PD extracts the digital signal from the optical carrier, and the detected photocurrent $y(t)$ is processed at the digital receiver. The optical signals travel between waveguides and wireless medium without the need for electro-optical conversion, thus avoiding additional delays and rate penalties.

In this paper, we focus on the OW links in hybrid NoC scenarios as shown in Fig. 1. In particular, OW links are partitioned into sets using the same carrier frequency. Recall that the reuse of optical wavelengths improves significantly the transport capacity of the OW NoC, since the number of simultaneous communications is not limited to the number of available wavelengths. We assume that all transmitting and receiving antennas are located on the same horizontal plane[1]. Fig. 3 shows the scenario of a set of OW links sharing the same optical carrier. In this figure, black and red dashed lines denote desired and interfering links for RX_0, respectively, and blue lines show other communication links. In the considered scenario with $I + 1$ transmitters, there is only one desired transmitter TX_0 for the probe receiver RX_0, and the other I transmitters $\text{TX}_1, \text{TX}_2, \cdots, \text{TX}_I$ cause interference to RX_0, while communicating with their corresponding receivers. The optical power[2] of the received desired signal is denoted by $P_0 = P_s$, and the optical power of the i-th received interfering signal, normalized to the desired optical power, is denoted by $x_i = P_i/P_0$, with $i = 1, 2, \cdots, I$. The received powers are functions of the geometrical parameters of the network. The distance between the antennas of RX_0 and TX_i is denoted by d_i. The angle between RX_0 antenna axis and the direction of signal received from TX_i antenna is given by $\theta_{0,i}$, and the angle between TX_i antenna axis and the direction of signal

---

[1]For the sake of simplicity in the presentation, we consider a two-dimensional network, but the analysis can be applied to three-dimensional scenarios as well.

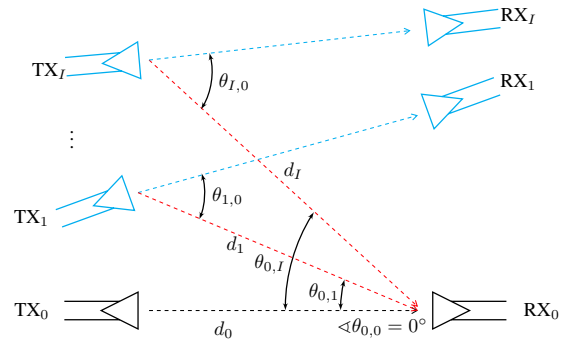[2]Here, optical power refers to the power of the unmodulated optical carrier.

Figure 3. The scenario of multiple OW links. Black and red dashed lines denote desired and interfering links for RX_0, respectively, and blue lines show other communication links.

transmitted to RX_0 antenna is denoted by $\theta_{i,0}$. The optical power received from TX_i can be modeled as [6]

$$P_i = C\, G_{\text{RX}_0}(\theta_{0,i}, \alpha_{0,i})\, G_{\text{TX}_i}(\theta_{i,0}, \alpha_{i,0})\, d_i^{-\beta} \qquad (1)$$

where the transmit antenna gain $G_{\text{TX}_i}(\cdot)$ and receive antenna gain $G_{\text{RX}_0}(\cdot)$ are functions of transmitting and receiving directions expressed by the angles θ and α in the three-dimensional space, β is the power-decay exponent and C is a coefficient that accounts for the transmit power, carrier wavelength and physical structure of the wireless medium. Therefore, the normalized interference power x_i in the two-dimensional scenario of Fig. 3, is given by

$$x_i(\theta_{0,i}, \theta_{i,0}, \rho) = \rho^2\, \frac{G_{\text{TX}_i}(\theta_{i,0})\, G_{\text{RX}_0}(\theta_{0,i})}{G_{\text{TX}_0}(\theta_{0,0})\, G_{\text{RX}_0}(\theta_{0,0})} \qquad (2)$$

with $\rho = d_0/d_i$ and assuming $\beta = 2$. In the desired link, the transmitting and receiving antennas are aligned, hence $\theta_{0,0} = 0°$.

III. COMMUNICATION LINK MODEL

The desired signal received at the time instant t is $E_0(t) = \sqrt{P_s}\, m_0(t)\, e^{j\omega t + j\phi_0(t)}$, and the i-th interfering signal is $E_i(t) = \sqrt{P_s\, x_i}\, m_i(t)\, e^{j\omega t + j\phi_i(t)}$, where ω is the carrier frequency. The phase fluctuations in the i-th transmitter are denoted by $\phi_i(t)$, and $m_i(t)$ represents the modulating data signal. We assume that all links use intensity modulation on-off keying (OOK), with binary modulating signals given by

$$m_0(t) = \sum_{n=-\infty}^{+\infty} b_{0,n}\, g(t - nT) \qquad (3a)$$

$$m_i(t) = \sum_{n=-\infty}^{+\infty} b_{i,n}\, g(t - nT - \tau_i) \qquad (3b)$$

where $b_{0,n}$ and $b_{i,n}$ are the n-th bits transmitted by the desired and i-th interfering sources, respectively. $g(t)$ is the rectangular shape of the optical pulse, T is the time interval for each bit, and τ_i is the time offset of the i-th asynchronous interfering link.

The detected photocurrent at the receiver is $y(t) = \eta\,|E_0(t) + \sum_{i=1}^{I} E_i(t)|^2$, which is given by

$$y(t) = \eta P_{\mathrm{s}}\Big[m_0(t) + 2\sum_{i=1}^{I} \sqrt{x_i}\, m_0(t)\, m_i(t)\cos\phi_i(t)$$
$$+ \sum_{i=1}^{I}\sum_{q=1}^{I} \sqrt{x_i\, x_q}\, m_i(t)\, m_q(t)\, e^{j(\phi_i - \phi_q)} \Big] \tag{4}$$

where η is the responsivity of the PD. In (4), the first sum accounts for the beating between desired and interference signals, and the second sum represents the self-beating of interfering signals. Note that in the literature on crosstalk analysis [33], [35], [37], [38], all the self-beating terms are often neglected. In order to derive a closed-form expression for BEP, we assume that the crossed terms with $i \neq q$ in the second sum of (4) are negligible, since these terms are very small for $x_i < 1$. Neglecting the crossed terms is equivalent to approximating the second sum of (4) with its average over ϕ_i's, thus obtaining

$$y(t) \cong \eta P_{\mathrm{s}}\Big[m_0(t) + 2\sum_{i=1}^{I} \sqrt{x_i}\, m_0(t)\, m_i(t)\cos\phi_i(t)$$
$$+ \sum_{i=1}^{I} x_i\, m_i(t) \Big]. \tag{5}$$

We assume that the spectrum of the unmodulated carrier is narrow with respect to $1/T$, meaning that the phase fluctuations are slow and remain approximately constant during the bit interval T. Therefore, the received photocurrent, after electrical filtering and sampling, is given by

$$\mathrm{I}^{(n)} = A_0\, b_{0,n} + \sum_{i=1}^{I} A_i \cos(\phi_i)\, b_{0,n}\, h(\tau_i, b_{i,n}, b_{i,n-1}) \tag{6}$$
$$+ \sum_{i=1}^{I} B_i\, h(\tau_i, b_{i,n}, b_{i,n-1})$$

where $A_0 = \eta\, P_{\mathrm{s}}$, $A_i = 2\sqrt{x_i}\,\eta\, P_{\mathrm{s}}$, $B_i = x_i\,\eta\, P_{\mathrm{s}}$. The function $h(\tau_i, b_{i,n}, b_{i,n-1})$ for the integrate-and-dump filter (IDF) is defined as

$$h(\tau_i, b_{i,n}, b_{i,n-1}) = \frac{1}{T_{\mathrm{g}}} \int_{nT}^{nT+T_{\mathrm{g}}} m_i(t)\, dt \tag{7}$$

where T_{g} is the rectangular pulse duration (see Fig. 4). Here, for non-return-to-zero (NRZ) transmission $T_{\mathrm{g}} = T$, whereas for return-to-zero (RZ) transmission $T_{\mathrm{g}} < T$ [42]. In particular, $h(\tau_i, b_i, \tilde{b}_i)$ is given by[3]

$$h(\tau_i, b_i, \tilde{b}_i) = \begin{cases} \tilde{b}_i \frac{\tau_i - T + T_{\mathrm{g}}}{T_{\mathrm{g}}} & \text{if}\quad T - T_{\mathrm{g}} \leq \tau_i \leq T \\ 0 & \text{otherwise} \end{cases}$$
$$+ \begin{cases} b_i \frac{T_{\mathrm{g}} - \tau_i}{T_{\mathrm{g}}} & \text{if}\quad 0 \leq \tau_i \leq T_{\mathrm{g}} \\ 0 & \text{otherwise} \end{cases} \tag{8}$$

which for the NRZ modulation scheme becomes

$$h(\tau_i, b_i, \tilde{b}_i) = \tilde{b}_i \frac{\tau_i}{T} + b_i \frac{T - \tau_i}{T}. \tag{9}$$

[3]For the sake of simplicity, we omit the sample index n, so $b_{0,n}$ is denoted by b_0, and $b_{i,n}$ and $b_{i,n-1}$ by b_i and $\tilde{b}_i$, respectively.
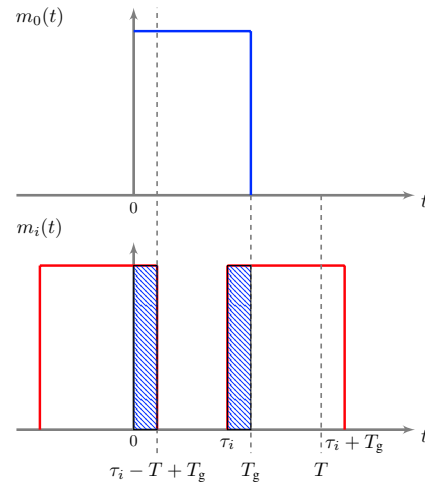

Figure 4. Asynchronous data signals. The area of the shaded region is given by $T_{\mathrm{g}} h(\tau_i, b_i, \tilde{b}_i)$.

The photocurrents in (6) for data $b_0 = 0$ is given by

$$\mathrm{I}_0 = \sum_{i=1}^{I} B_i\, h(\tau_i, b_i, \tilde{b}_i) \tag{10a}$$

and for $b_0 = 1$ by

$$\mathrm{I}_1 = A_0 + \sum_{i=1}^{I} A_i \cos(\phi_i) h(\tau_i, b_i, \tilde{b}_i) + \sum_{i=1}^{I} B_i\, h(\tau_i, b_i, \tilde{b}_i). \tag{10b}$$

The bits $b_{i,n}$ are independent random variables (RVs) with one-half probability to be one or zero, and ϕ_i and τ_i are independent RVs uniformly distributed on $[0, 2\pi]$ and $[0, T]$, respectively. The vectors $\boldsymbol{\tau} = \{\tau_i\}$, $\boldsymbol{\phi} = \{\phi_i\}$, $\boldsymbol{b}_{\mathrm{I}} = \{b_i\}$, and $\tilde{\boldsymbol{b}}_{\mathrm{I}} = \{\tilde{b}_i\}$ have I elements, $i = 1, 2, \cdots, I$. We also consider additive Gaussian noise at the receiver denoted by $N \sim \mathcal{N}(0, \sigma_{\mathrm{th}}^2)$ with variance σ_{th}^2. In most cases of interest for p-i-n receivers, the dominant noise contribution is thermal noise [43], hence the noise has the same variance σ_{th}^2 independently of the photocurrent value (I_0 and I_1). Table I at the top of the next page summarizes the main parameters of the system model.

Remarks: When phase fluctuations are very fast, the spectrum of the unmodulated carrier is much larger than $1/T$ and the second term in (6) is averaged out by the receiver filter, which gives $A_i = 0$. Note that in the case of synchronous interference ($\tau_i = 0$), we have $h(\tau_i, b_i, \tilde{b}_i) = b_i$ in both the equations (8) and (9).

IV. ERROR PROBABILITY EVALUATION

The BEP is the probability that the received photocurrent is detected above a decision threshold ζ while transmitting *zero*, or is detected below ζ while transmitting *one*, which is written by

$$P_{\mathrm{b}} = \frac{1}{2}(P_{\mathrm{b}|b_0=0} + P_{\mathrm{b}|b_0=1})$$
$$= \frac{1}{2}(\mathbb{P}\{\mathrm{I}_0 + N \geq \zeta\} + \mathbb{P}\{\mathrm{I}_1 + N < \zeta\}). \tag{11}$$

Table I. System model parameters.

G	antenna Gain	$b_{i,n}$	n-th bit transmitted by TX_i
T	bit interval	$\phi_i(t)$	phase fluctuations of TX_i
T_g	rectangular pulse duration	τ_i	time offset of TX_i
I	number of interferers	B_i	self-beating factor of the i-th interferer
P_i	i-th signal power	η	responsivity of PD
x_i	i-th normalized interference power	σ_{th}	noise standard deviation
d_i	distance between TX_i and RX_0 antennas	γ	$A_0/(2\sigma_{th})$ with $A_0 = \eta P_0$

First, we consider the conditional BEP, $P_{b|\tau,b_I,\tilde{b}}$, for given vectors τ, b_I and $\tilde{b}$. Then, the conditional BEP is averaged with respect to b_I and $\tilde{b}$ as

$$P_{b|\tau} = \mathbb{E}_{b_I,\tilde{b}_I}\{P_{b|\tau,b_I,\tilde{b}_I}\} = \frac{1}{2^{2I}}\sum_{(b_I,\tilde{b}_I)\in\mathcal{B}} P_{b|\tau,b_I,\tilde{b}_I} \quad (12)$$

where all the 2^{2I} combinations of $(b_I,\tilde{b}_I)\in\mathcal{B}$ are considered, and $\mathcal{B} = \{(b_i,\tilde{b}_i) : b_i = \{0,1\}, \tilde{b}_i = \{0,1\}\}$.

Therefore, by substituting (10) in (11), the conditional BEP is given by

$$P_{b|\tau,b_I,\tilde{b}_I} = \frac{1}{2}(P_{b|b_0=0,\tau,b_I,\tilde{b}_I} + P_{b|b_0=1,\tau,b_I,\tilde{b}_I}) \quad (13)$$

where

$$P_{b|b_0=0,\tau,b_I,\tilde{b}_I} = \mathbb{P}\Big\{\sum_{i=1}^{I} B_i\, h(\tau_i,b_i,\tilde{b}_i) + N > \zeta\Big\}$$
$$= \mathbb{P}\Big\{n > \Big(\zeta - \sum^{N} B_i\, h(\tau_i,b_i,\tilde{b}_i)\Big)/\sigma_{th}\Big\} \quad (14a)$$

$$P_{b|b_0=1,\tau,b_I,\tilde{b}_I} = \mathbb{P}\Big\{A_0 + \sum_{i=1}^{I} A_i\cos(\phi_i)h(\tau_i,b_i,\tilde{b}_i)$$
$$+ \sum_{i=1}^{I} B_i\, h(\tau_i,b_i,\tilde{b}_i) + N < \zeta\Big\}$$
$$= \mathbb{P}\Big\{\sum_{i=1}^{I} A_i\cos(\phi_i)h(\tau_i,b_i,\tilde{b}_i)/\sigma_{th} + n <$$
$$\Big(\zeta - A_0 - \sum_{i=1}^{I} B_i\, h(\tau_i,b_i,\tilde{b}_i)\Big)/\sigma_{th}\Big\} \quad (14b)$$

and $n = N/\sigma_{th}$ is a Gaussian RV with unitary variance. The conditional probabilities in (13), $P_{b|b_0=0,\tau,b_I,\tilde{b}_I}$ and $P_{b|b_0=1,\tau,b_I,\tilde{b}_I}$, can be obtained through a general parametric expression as given by

$$P_{b|b_0,\tau,b_I,\tilde{b}_I} = F(\mathbf{u}^{(b_0)}, v^{(b_0)})$$
$$= \mathbb{P}\Big\{\sum_{i=1}^{I} u_i^{(b_0)}\cos(\phi_i) + n > v^{(b_0)}\Big\}$$
$$= \mathbb{P}\Big\{\sum_{i=1}^{I} u_i^{(b_0)}\cos(\phi_i) + n < -v^{(b_0)}\Big\}$$
$$= \frac{1}{2(2\pi)^I}\int_0^{2\pi}\cdots\int_0^{2\pi}\operatorname{erfc}\Big[\frac{v^{(b_0)} + \sum_{i=1}^{I} u_i^{(b_0)}\cos(\phi_i)}{\sqrt{2}}\Big]$$
$$\times d\phi_1\cdots d\phi_I \quad (15)$$

where $v^{(b_0)}$ and the elements of vector $\mathbf{u}^{(b_0)} = \{u_i^{(b_0)}, i = 1,2,\ldots,I\}$ are defined as

$$v^{(b_0)} = \begin{cases} (\zeta - \sum_{i=1}^{I} B_i h(\tau_i,b_i,\tilde{b}_i))/\sigma_{th} & \text{if } b_0 = 0 \\ (-\zeta + A_0 + \sum_{i=1}^{I} B_i\, h(\tau_i,b_i,\tilde{b}_i))/\sigma_{th} & \text{if } b_0 = 1 \end{cases} \quad (16a)$$

and

$$u_i^{(b_0)} = \begin{cases} 0 & \text{if } b_0 = 0 \\ A_i h(\tau_i,b_i,\tilde{b}_i)/\sigma_{th} & \text{if } b_0 = 1 \end{cases} \quad (16b)$$

respectively. Note that in (14a), the beating between desired and interference signals has no impact on the desired signal when $b_0 = 0$, therefore, $u_i^{(0)} = 0$, $\forall i$.

In the presence of single interferer ($I = 1$), by using [40, eq. (5)], an exact closed-form expression for (15) can be derived as

$$F(u_1^{(b_0)}, v^{(b_0)}) = \frac{1}{2}\operatorname{erfc}\Big(\frac{v^{(b_0)}}{\sqrt{2}}\Big) + \frac{1}{\sqrt{2\pi}}\sum_{k=1}^{\infty}\Big\{\Big(\frac{u_1^{(b_0)}}{2}\Big)^{2k}$$
$$\times \frac{1}{(k!)^2}H_{2k-1}(v^{(b_0)})\exp(-(v^{(b_0)})^2/2)\Big\} \quad (17)$$

where $H_z(x) = (-1)^z e^{-x^2/2}(d^z e^{-x^2/2}/dx^z)$ is a Hermitian polynomial of order z. Although the equation (17) provides an exact BEP, due to convergence issues of the sum with index k, its numerical evaluation is extremely difficult for large values of desired and interfering signals powers (P_s and x_i) in interference-limited conditions.

The expression in (15) can be approximated for $I \geq 1$ by extending the approach in [37], where the probability density function (PDF) of the noise photocurrent was derived based on a truncated Taylor series with respect to ϕ_i's. By applying [37, eq. (5)] to the considered system model, (15) can be approximated by

$$F(\mathbf{u}^{(b_0)}, v^{(b_0)}) \simeq \frac{1}{2}\operatorname{erfc}\Big(\frac{v^{(b_0)} - \sum_{m=1}^{I} u_m^{(b_0)}}{\sqrt{2}}\Big)$$
$$\times \prod_{i=1}^{I}\mathcal{G}(u_i^{(b_0)}(v^{(b_0)} - \sum_{m=1}^{I} u_m^{(b_0)})) \quad (18)$$

where

$$\mathcal{G}(z) = \begin{cases} 1 & \text{if } z = 0 \\ \frac{1}{\sqrt{2\pi z}}\operatorname{erf}(\pi\sqrt{z/2}) & \text{if } z > 0 \end{cases} \quad (19)$$

which is valid for $v^{(b_0)} - \sum_{m=1}^{I} u_m^{(b_0)} \geq 0$. In the case of $I = 1$, (18) can be evaluated for a larger domain of P_s and x_i values with respect to the domain for which (17) can

be calculated exactly. The accuracy of the approximate BEP with respect to its exact evaluation is verified by results in Section V. Therefore, for a given threshold ζ, the exact $P_{b|\tau}$ with $i = 1$ and approximate $P_{b|\tau}$ with $i \geq 1$ are evaluated by substituting (17) and (18) in the equation (13), respectively. The exact BEP for $i \geq 1$ is evaluated numerically by the proposed method in Appendix C.

We now apply two methods, namely AOP and MoE, to set the decision thresholds. The AOP threshold is determined from the average value of the received photocurrent, which is given by

$$\zeta_{avg} = \frac{\mathbb{E}\{I_0\} + \mathbb{E}\{I_1\}}{2} = A_0/2 + \sum_{i=1}^{I} B_i \overline{h} \qquad (20)$$

with

$$\overline{h} = \mathbb{E}_{\tau_i, b_i, \tilde{b}_i}\{h(\tau_i, b_i, \tilde{b}_i)\} = \frac{1}{4T} \sum_{b_i=0}^{1} \sum_{\tilde{b}_i=0}^{1} \int_0^T h(\tau_i, b_i, \tilde{b}_i) d\tau_i$$

$$= \frac{1}{4T} \sum_{b_i=0}^{1} \sum_{\tilde{b}_i=0}^{1} \frac{T_g}{2}(b_i + \tilde{b}_i) = \frac{T_g}{2T}. \qquad (21)$$

The MoE threshold is set at the middle of the eye diagram in the worst case of maximum eye closure, i.e., when the impact of interference on the desired signal is the maximum. In such case, the threshold is defined as

$$\zeta_{moe} = \frac{\max\{I_0\} + \min\{I_1\}}{2} = A_0/2 + \sum_{i=1}^{I}(B_i - A_0\sqrt{x_i}). \qquad (22)$$

By applying AOP and MoE thresholds, the conditional BEP, $P_{b|\tau}(\gamma, \mathbf{x})$, is provided in Appendix A and Appendix B, respectively, as a function of the electrical SNR, with SNR $= 4\gamma^2$ and $\gamma = A_0/(2\sigma_{th})$, and the vector $\mathbf{x}$.

A. BEP for asynchronous and quasi-synchronous systems

In this work, the system is considered asynchronous, when the transmission interval (TI), i.e., time slot or protocol time unit, is large with respect to the variations of time offsets (τ). Therefore, the beating between desired and interfering signals is subject to the variations of τ_i's, and the BEP is averaged with respect to τ. We consider the system quasi-synchronous, when the time scale of τ variations is larger than TI. In this case, τ can be assumed constant over each TI, and the system experiences a BEP conditioned to τ, which changes randomly for different TIs in a range of $[P_{b,min}, P_{b,max}]$. The system is synchronous, when $\tau_i = 0$, $\forall i$, which has been mostly considered in the literature on optical crosstalk. Therefore, in the asynchronous system with $I = 1$, the BEP is given by

$$P_b(\gamma, x_1) = \frac{1}{T} \int_0^T P_{b|\tau_1}(\gamma, x_1) \, d\tau_1 \qquad (23)$$

and for $I > 1$ is given by averaging $P_{b|\tau}(\gamma, \mathbf{x})$ with respect to the vector τ as

$$P_b(\gamma, \mathbf{x}) = \frac{1}{T^I} \int_0^T \cdots \int_0^T P_{b|\tau}(\gamma, \mathbf{x}) \, d\tau_1 \cdots d\tau_I \qquad (24)$$
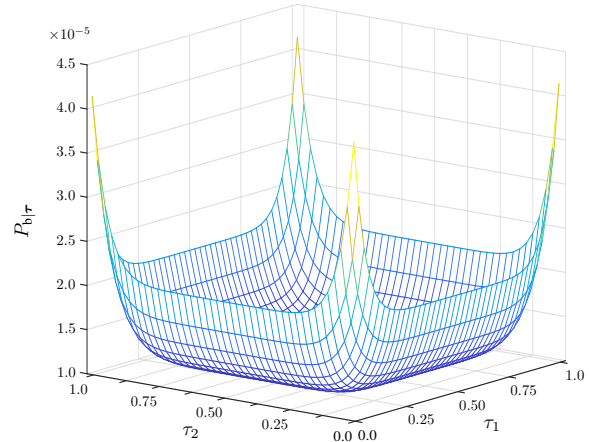

Figure 5. The conditional BEP $P_{b|\tau}(\gamma, \mathbf{x})$ vs. τ_1, τ_2 with $I = 2$, AOP threshold, $\gamma = 15$, $x_1 = x_2 = -19$ dB and NRZ modulation.
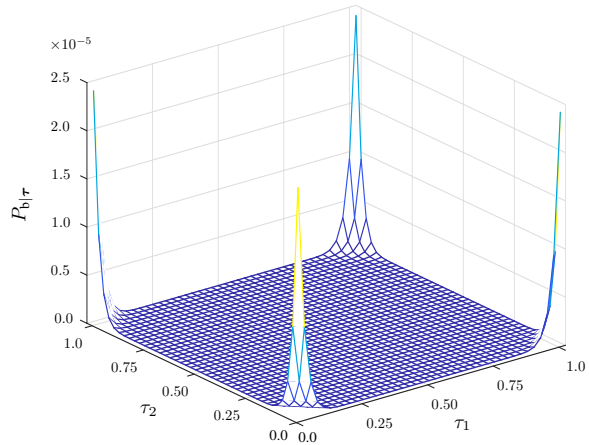

Figure 6. The conditional BEP $P_{b|\tau}(\gamma, \mathbf{x})$ vs. τ_1, τ_2 with $I = 2$, AOP threshold, $\gamma = 15$, $x_1 = x_2 = -19$ dB and RZ modulation.

where $P_{b|\tau}(\gamma, \mathbf{x})$ for the AOP and MoE thresholds is given by (36) and (40), respectively.

In the quasi-synchronous system, the behavior of $P_{b|\tau}(\gamma, \mathbf{x})$ as a function of time offsets (τ) is examined for the two cases of NRZ and RZ pulse shaping. An illustrative example of the system with $I = 2$ is shown in Fig. 5 for NRZ modulation, and in Fig. 6 for RZ modulation, where the conditional BEP as a function of τ_1 and τ_2 is provided. The AOP threshold and $\gamma = 15$ are considered with $x_1 = x_2 = -19$ dB. In both figures, it is shown that the highest BEP, $P_{b,max}$, is achieved when $\tau_i = 0$, $\forall i$, whereas the lowest BEP, $P_{b,min}$, is achieved when $\tau_i = T/2$, $\forall i$. This behavior allows a simple evaluation of $P_{b,min}$ and $P_{b,max}$ and it is valid for various system settings, except for the case with high level of interference that causes

eye diagram closure. By comparing the two figures, it can be observed that the system with RZ modulation is less sensitive to the interference than that with NRZ modulation.

In Section IV-B, we propose a simple closed-form formula to approximate (23) and (24) by considering the particular shape of $P_{\mathsf{b}|\boldsymbol{\tau}}(\gamma, \mathbf{x})$ as the function of τ_i's values.

B. BEP approximation for asynchronous systems

Consider the behavior of $P_{\mathsf{b}|\boldsymbol{\tau}}$ as a function of τ_i's in Section IV-A with $P_{\mathsf{b}|\boldsymbol{\tau}} = p(\tau_1, \tau_2, \ldots, \tau_I)$. Therefore, $P_{\mathsf{b,min}} = p(\tau_1, \ldots, \tau_I)$ with $\tau_i = T/2, \forall i$, and $P_{\mathsf{b,max}} = p(\tau_1, \ldots, \tau_I)$ with $\tau_i = 0, \forall i$. We assume that the function $p(\cdot)$ is concave and symmetric for given τ_i's, i.e., $p(\ldots, \tau_i, \ldots) = p(\ldots, T - \tau_i, \ldots), \forall i$. In such case, the BEP in (24) can be written as

$$P_{\mathsf{b}}(\gamma, \mathbf{x}) = \frac{2^I}{T^I} \int_0^{T/2} \cdots \int_0^{T/2} p(\tau_1, \ldots, \tau_I)\, d\tau_1 \cdots d\tau_I. \tag{25}$$

In order to evaluate the integrals in (25), the function $p(\cdot)$ can be approximated with the composition of two I-dimensional hyperplanes. The first plane is horizontal and is given by $p_1(\tau_1, \ldots, \tau_I) = P_{\mathsf{b,min}}$. The second plane crosses the function $p(\cdot)$ at the point $(\tau_1 = 0, \ldots, \tau_I = 0)$ and is given by $p_2(\tau_1, \ldots, \tau_I) = P_{\mathsf{b,max}} - \sum_{i=1}^I \mu_i \tau_i$, where the parameters μ_i are obtained[4] by $\mu_i = \partial p(\tau_1, \ldots, \tau_I)/\partial \tau_i|_{\tau_1 = \ldots = \tau_I = 0}$. The intersection of these two planes is an $(I - 1)$-dimensional hyperplane given by $\sum_{i=1}^I \mu_i \tau_i = P_{\mathsf{b,max}} - P_{\mathsf{b,min}} = \Delta_{\mathsf{P}}$ in implicit form. Thus, function $p(\cdot)$ can be approximated by

$$p(\tau_1, \ldots, \tau_I) \approx \max\left(p_1(\tau_1, \ldots, \tau_I), p_2(\tau_1, \ldots, \tau_I)\right) \tag{26}$$

$$= P_{\mathsf{b,min}} + \max\left(0, \Delta_{\mathsf{P}} - \sum_{i=1}^I \mu_i \tau_i\right).$$

Finally, an approximation to the BEP can be provided by using (25) and (26), which for $I = 1$ is given by

$$P_{\mathsf{b}}(\gamma, x_1) \approx P_{\mathsf{b,min}} + \frac{\Delta_{\mathsf{P}}^2}{T \mu_1} \tag{27}$$

and for arbitrary value of I is given by

$$P_{\mathsf{b}}(\gamma, \mathbf{x}) \approx P_{\mathsf{b,min}} + \frac{2^I \Delta_{\mathsf{P}}^{I+1}}{T^I (I+1)! \prod_{i=1}^I \mu_i}. \tag{28}$$

V. NUMERICAL RESULTS

This section provides numerical results in terms of BEP for NoCs using OW links in the presence of cochannel interference and noise. Synchronous and asynchronous networks are considered, where all optical links use OOK modulation with NRZ and RZ formats. The exact BEP for $I = 1$ is evaluated by (23), where conditional BEP ($P_{\mathsf{b}|\tau_1}$) with AOP and MoE thresholds is given by (34) and (39), respectively. The approximate BEP for $I \geq 1$ is evaluated by (24), where conditional BEP ($P_{\mathsf{b}|\boldsymbol{\tau}}$) with AOP and MoE threshold is given by (36) and (40), respectively. The total normalized interference power is $X_{\mathsf{tot}} = \sum_i^I x_i$, and for the RZ modulation, $T_{\mathsf{g}} = 0.5 \times T$ is considered.

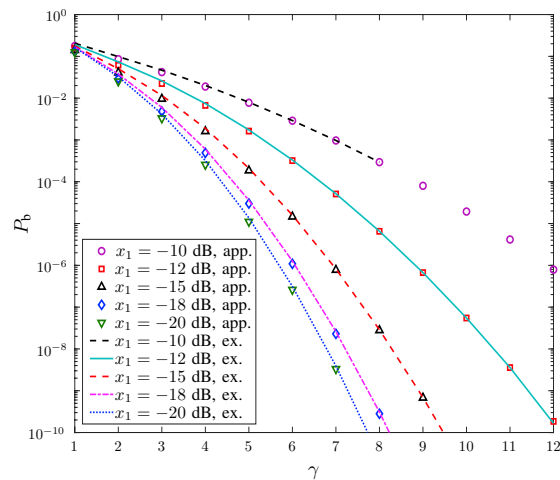[4]This evaluation can be performed numerically.

Figure 7. BEP vs. γ for asynchronous systems with NRZ modulation, single interferer and different values of x_1 using approximate and exact methods, and MoE threshold. Lines and symbols show exact and approximate BEP, respectively.

A. BEP of OW links

We now present results for different system settings by using the formulas derived in Section IV.

Fig. 7 shows the exact and approximate BEP as a function of γ in the presence of one interfering transmitter. The asynchronous system with NRZ modulation and MoE threshold is considered for different values of x_1. The lines refer to the exact BEP, while symbols indicate the approximate BEP. The results exhibit a good agreement between the exact and approximate BEP. Therefore, for the BEP evaluation, approximate method can be used instead of the exact one, since the approximate evaluation compared to the exact evaluation, is simpler and numerically calculable for high values of γ and x_1, and also for $I > 1$. For example, for $x_1 = -10$ dB and $\gamma > 8$, the evaluation of (39) with Matlab or Mathematica tools become numerically unstable, whereas the approximate BEP is obtained by (40) without problems for $\gamma > 8$. It can be also observed that by reducing the value of x_1, the distances between curves reduce, since the results approach the asymptotic limit for small values of x_1, i.e., noise-limited system.

Fig. 8 shows the BEP as a function of γ for different numbers of interferers with RZ and NRZ modulation schemes. The power of interfering signals, x_1, x_2 and x_3, are selected such that the total power for all curves is -16 dB, where for $I = 1$, $x_1 = -16$ dB, for $I = 2$, $\mathbf{x} = [-17, -23]$ dB, and for $I = 3$, $\mathbf{x} = [-18, -22, -26]$ dB. Solid lines show RZ case and dashed lines show NRZ case. It is shown that for a given number of interferers and γ, RZ outperforms NRZ. For example, the BEP with $I = 3$ and NRZ shows an asymptotic floor that approaches 10^{-3}, whereas by exploiting RZ the floor decreases drastically achieving 2×10^{-8} at $\gamma = 20$. It can be also observed that for a given modulation scheme and γ, the BEP increases as interferers number (I) increases independently of the amount of total interference power. Note
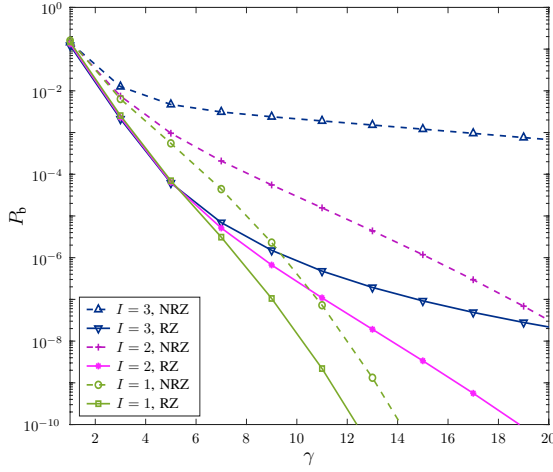
Figure 8. BEP vs. γ with RZ and NRZ modulation schemes and $X_{\text{tot}} = -16$ dB for $I = 1, 2$ and 3 using AOP threshold.
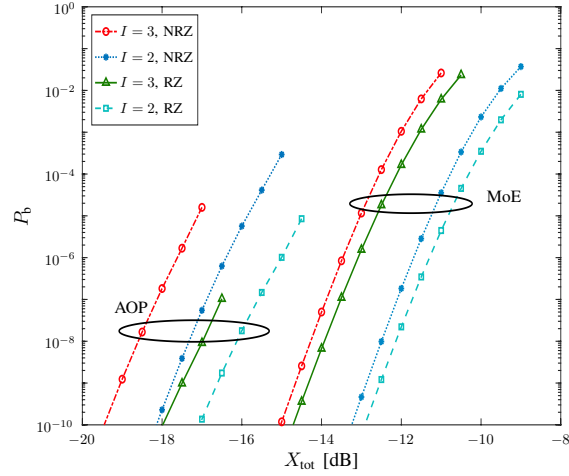

Figure 10. BEP vs. X_{tot} in dB for RZ and NRZ modulation schemes with $I = 2$ and 3, and $\gamma = 15$, using AOP and MoE thresholds.
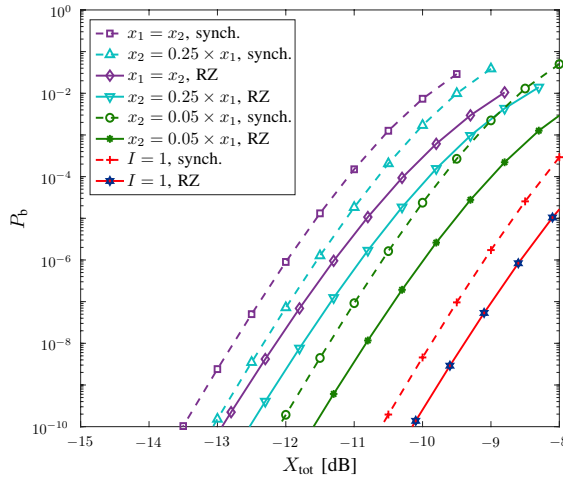

Figure 9. BEP vs. X_{tot} in dB for synchronous systems and asynchronous systems using RZ modulation with $I = 1$ and 2, $\gamma = 15$, and MoE threshold.
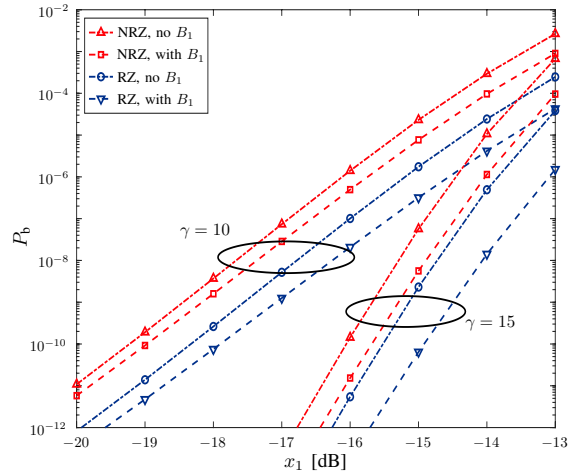

Figure 11. BEP vs. x_1 in dB for an asynchronous systems using RZ and NRZ modulation schemes, $I = 1$ and AOP threshold, with and without contribution of B_1 in (6).

that the higher is the number of interferers, the higher is the gap between RZ and NRZ curves. Therefore, for a given X_{tot}, by increasing I, the sensitivity of the system to the modulation scheme increases.

B. BEP as a function of interference power

In the following, we set the value of γ to 15 for an interference-limited network, and examine the BEP as the function of total normalized interference power (X_{tot}), varying thresholds and other system parameters. The results allow the system designer to determine the amount of interference the desired link can tolerate without exceeding a target BEP.

Fig. 9 shows the BEP vs. X_{tot} for synchronous and asynchronous systems with RZ modulation, $I = 1$ and 2 applying

MoE threshold. For $I = 2$, the two cases of equal power interference with $x_1 = x_2$, and unequal power distribution between interferers with $x_2 = 0.25 \times x_1$ and $x_2 = 0.05 \times x_1$ are examined. It can be observed that increasing the difference between x_1 and x_2 ameliorates the BEP, which gets closer to the case of single dominant interferer i.e., $I = 1$. Therefore, for a given X_{tot}, an upper bound and a lower bound for the BEP can be obtained with equal power interference and single dominant interferer cases, respectively. It is also shown that for each setting, synchronous case results in a higher BEP with respect to the asynchronous one (RZ).

Fig. 10 shows the BEP vs. X_{tot} for RZ and NRZ modulation schemes with different numbers of interferers using AOP and MoE thresholds. The cases $I = 2$ and 3 are examined, where
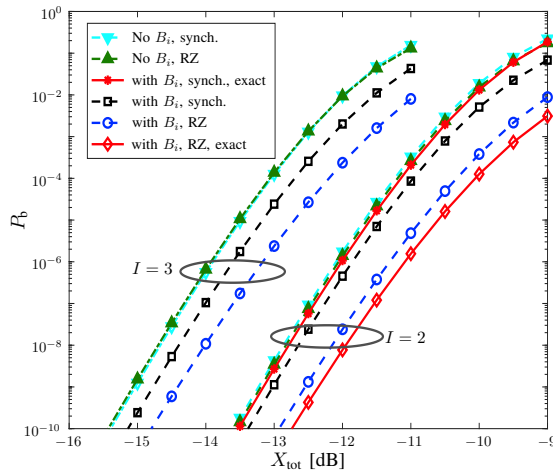
Figure 12. BEP vs. X_{tot} in dB for synchronous and asynchronous (RZ) systems, different numbers of interferers, $\gamma = 15$ and MoE threshold, with and without contribution of B_i's in (6).

Figure 13. BEP vs. X_{tot} in dB for asynchronous systems with NRZ modulation, $I = 3$, $\gamma = 15$, and AOP and MoE thresholds.

$x_2 = 0.5 \times x_1$ and $x_3 = 0.75 \times x_1$. This figure provides a comparison between two types of thresholds; it is shown that the MoE curves outperform the AOP ones for all settings. For example, the system using MoE with $I = 2$ and NRZ can reach $P_{\text{b}} = 10^{-9}$ for $x = -13$ dB, while the system with the same setting but using AOP satisfies such P_{b} for $x = -18$ dB. It can be also observed that for the same value of interference (X_{tot}), the lower I provides smaller BEP in both cases of AOP and MoE thresholds. The implementation of the MoE threshold requires more effort than AOP one, since the AOP threshold can be simply determined by the average of the received photocurrent. Therefore, it is suitable to use the MoE threshold, when the performance is improved significantly.

In Fig. 11, the BEP is plotted as a function of x_1 for asynchronous systems with RZ and NRZ modulations, $I = 1$, $\gamma = 10$ and 15, and AOP threshold. This figure examines the impact of self-beating interference signal (B_1 in equation (6)) on the BEP. Note that in the presence of single interferer, there is no crossed term ($i \neq q$ in the second sum of (4)) in the self-beating contribution of interference. As seen, for both modulation schemes, accounting for self-beating term (B_1) leads to a reduced BEP. We conclude that self-beating interference can influence the system performance, whereas many works in literature like [37], [40] have neglected this contribution. It can be also observed that, for a given modulation scheme and x_1, the gap between curves "with B_1" and "no B_1" increases as the value of γ increases.

Fig. 12 shows the BEP vs. X_{tot} with $I = 2$ and 3, where $x_2 = 0.5 \times x_1$ and $x_3 = 0.75 \times x_1$, using MoE threshold. For each I, four settings are examined (dashed lines) with and without contribution of self-beating interference (B_i's) in the synchronous and asynchronous (RZ) systems. It can be observed that by neglecting the contribution of B_i's, the synchronous and RZ cases are almost overlapped, and the
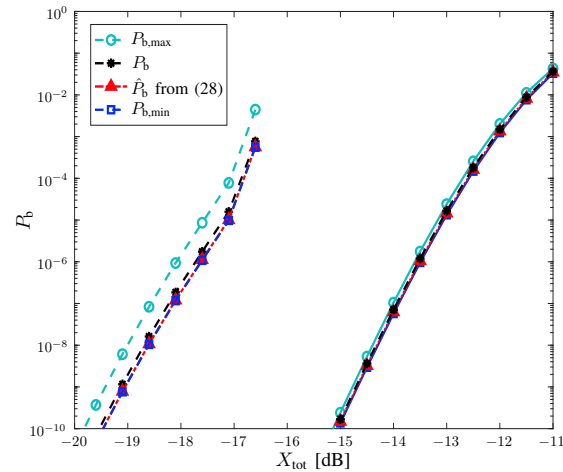
BEP is not improved with asynchronous transmission (RZ). But, considering B_i's provides a lower BEP for RZ case with respect to the synchronous one, and improves the BEP in both the synchronous and RZ cases. In order to verify the approximation in (5), where the beating of two different interfering signals (crossed-terms with $i \neq q$) is neglected, an exact evaluation of the BEP is also provided for synchronous and RZ cases with $I = 2$ (solid red lines). The exact BEP is calculated numerically through the method in Appendix C. It is shown that the exact P_{b} is lower than its approximation for the asynchronous RZ case, and is higher than its approximation for the synchronous case. As seen for the RZ case, the approximation results in a worst case evaluation of the BEP. Therefore, for the asynchronous case with RZ, a system designer can rely on the slightly greater value of the approximate BEP to guarantee the target BEP.

Fig. 13 compares different evaluation methods of the BEP vs. X_{tot} for asynchronous systems with $I = 3$, $x_2 = 0.5 \times x_1$ and $x_3 = 0.75 \times x_1$, using AOP and MoE thresholds. The results for $P_{\text{b,max}} = \max\{P_{\text{b}}\}$ and $P_{\text{b,min}} = \min\{P_{\text{b}}\}$ are given by $P_{\text{b}|\tau_1=\tau_2=...=\tau_I=0}(\gamma, x)$ and $P_{\text{b}|\tau_1=\tau_2=...=\tau_I=T/2}(\gamma, x)$, respectively, where $P_{\text{b}|\tau}$ with AOP is evaluated by (36), and with MoE by (40). P_{b} is evaluated by averaging $P_{\text{b}|\tau}$ in (24), whose approximation, $\hat{P}_{\text{b}}$, is provided through (28). It can be observed that for the MoE threshold, $\hat{P}_{\text{b}}$ and P_{b} are almost overlapping, and are very closed to $P_{\text{b,min}}$ and $P_{\text{b,max}}$. For the AOP threshold, the estimated $\hat{P}_{\text{b}}$ approximately overlaps $P_{\text{b,min}}$ and P_{b}, while there is an observable gap between $P_{\text{b,max}}$ and the other curves. However, in asynchronous systems, the proposed method in (28) can provide a good estimation of P_{b} with high accuracy for both types of thresholds.

C. Reuse distance for multiple OW links

Here, we apply the analytical framework in Section IV to analyze a particular scenario with parallel OW links as
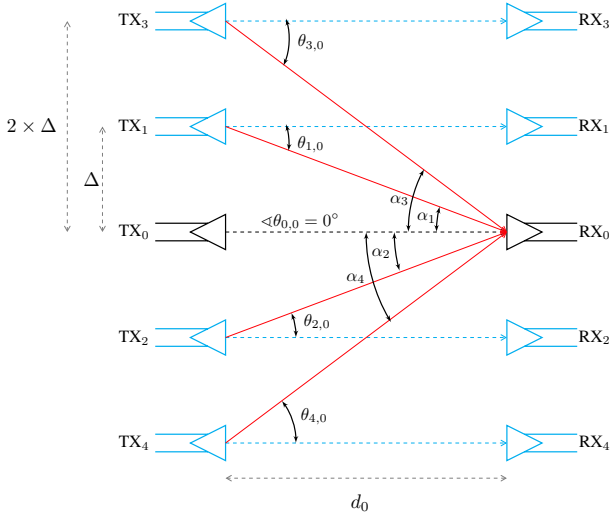
Figure 14. Network scenario with a set of parallel OW links using the same optical frequency ω. Black and red lines denote desired and interfering links for RX_0, respectively, and blue lines show other communication links.
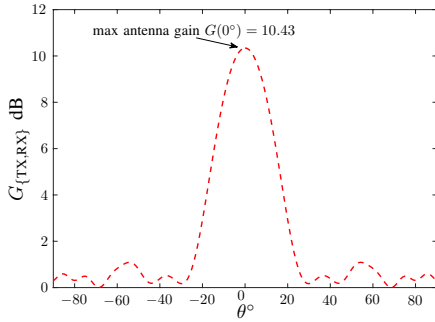

Figure 15. Antenna gain vs. horizontal radiation angle, according to the radiation pattern in [5].

illustrated in Fig. 14. The OW links operating at the same frequency are arranged such that adjacent links have equal distance from each other. We aim to determine how much reuse distance must be considered between the OW links satisfying a given BEP. Studying such scenario allows a simple evaluation of the reuse distance as a parametric function of the link length and SNR, which can be useful for regular grid-based designs. Other examples that apply the performance evaluation proposed in this work have been provided in [44], where real scenarios are investigated by using realistic parameters for antennas, receivers and transmitters, and a ray tracing modeling in the wireless channels.

In Fig. 14, black and red lines denote desired and interfering links for RX_0, respectively, and blue lines show other communication links. The transmitters $TX_0, \cdots , TX_4$ have parallel axes in bi-dimensional plane, thus $\theta_{0,i} = \theta_{i,0}$, where $\alpha_i = \theta_{0,i}$ in the figure. The distance between each i-th pair antennas TX_i-RX_i (link length) is denoted by d_0, and Δ is the distance between two adjacent links, i.e., the reuse distance of the links.
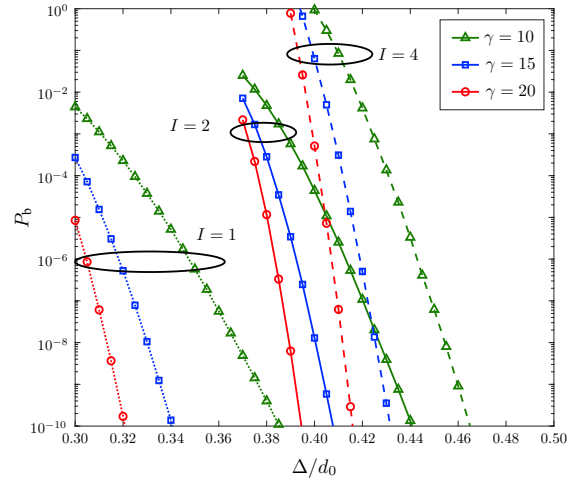

Figure 16. BEP vs. Δ/d_0 for the network scenario in Fig. 14, with asynchronous transmissions, NRZ modulation, $\gamma = 10$, 15 and 20, and different values of I using MoE threshold.

In such scenario, the equation (2) becomes

$$x_i = \frac{G_{TX_i}(\theta_{i,0})^2}{G_{TX_0}(\theta_{0,0})^2}(d_i/d_0)^{-2} . \qquad (29)$$

Note that for the 1-st and 2-nd TX-RX links, $\tan(\theta_{i,0}) = \Delta/d_0$ and for 3-rd and 4-th links, $\tan(\theta_{i,0}) = 2\Delta/d_0$. Here, the radiation pattern of the antenna in [5] is considered. Fig. 15 shows the antenna gain as a function of the angle (θ) between radiation direction and antenna axis, where the maximum antenna gain is $G(0) = 10.43$ dB.

Fig. 16 provides the BEP as a function of Δ/d_0 for some values of γ, i.e., 10, 15 and 20, in the scenario of Fig. 14, where asynchronous case with NRZ modulation, MoE threshold and different numbers of interfering transmitters are considered. In the case of $I = 1$, one of the adjacent transmitters, TX_1 or TX_2, is considered as the interfering source. For $I = 2$, both TX_1 and TX_2, and for $I = 4$, all transmitters except TX_0 are interfering with the desired link. For a given Δ/d_0, the values of x_i are obtained from (29), and P_b is evaluated through (28) with $P_{b|\tau}(\gamma, \mathbf{x})$ from (40). Fig. 16 shows high sensitivity of the BEP to the network geometry. As shown, the BEP changes drastically even with small changes of the reuse factor Δ/d_0, since the BEP does not depend only on the length of connection link, but also on the angles between antennas axes.

This kind of results enables us to design reuse distance and topology of wireless links satisfying a target BEP, i.e., guaranteeing reliable communication in NoCs. For example, given a target BEP of 10^{-8}, a set of 3 parallel OW links with $\gamma = 15$ can reuse the same optical carrier providing reliable communication, if the antennas spacing is at least 0.4 of the link length ($\Delta/d_0 = 0.4$). When design constraints lead to reduce antennas spacing as $\Delta/d_0 = 0.3$, the 3 parallel links cannot use the same optical carrier, thus at least 2 different optical carriers must be used in order to reach the target BEP. Moreover, the results like Fig. 16 allow us to understand the effect of network scaling. In particular, the increase of

network scale with growing the number of on-chip cores and interconnections, leads to a higher number of interfering links in the case of frequency reuse. In such case, the distance between OW links has to be increased to maintain a target BEP. Note that, as the number of interferers increases, the amount of the increase in reuse distance gets smaller and smaller, and tends to zero for a high number of interferers [37]. If we can support such small increase of reuse distance in the design of NoCs with high number of interferers, the reuse of optical carrier will increase the network capacity as the network scales up.

VI. CONCLUSIONS

The effects of cochannel interference on optical wireless communications (OW) for network-on-chips (NoCs) have been investigated. The BEP for synchronous, quasi-synchronous and asynchronous systems with return-to-zero (RZ) and non-return-to-zero (NRZ) modulation schemes has been derived by applying exact and tight approximation methods. Unlike most published works, the beating between interfering signals is also considered to provide an accurate performance evaluation. The proposed analysis can be applied to both noise- and interference-limited systems. In the numerical results, it is shown that the system robustness against interference increases with asynchronous transmission, RZ pulse shaping and suitable design of detection threshold. A case study with multiple on-chip OW links is also investigated, which shows how the proposed analysis can be exploited to evaluate the reuse distance between links operating on the same wireless channel. The framework helps a system designer to find an optimal layout for OW interconnects in NoCs that satisfies the BEP requirement. Future research directions may include the investigation of on-chip OW links performance using realistic channel modeling and antenna design, and the experimental verification of numerical findings. Moreover, further work is required to realize the full design of NoC architectures with OW links by considering the real characteristics of optical components and on-chip wireless channels, and BEP performance.

APPENDIX A
AVERAGED OPTICAL POWER (AOP) THRESHOLD

By applying ζ_{avg} to (16a), $v^{(b_0)}$ becomes

$$v^{(b_0)} = \begin{cases} \frac{A_0}{2\sigma_{\text{th}}} \lambda'(\boldsymbol{\tau}, \mathbf{b_I}, \tilde{\mathbf{b}}_\mathbf{I}) & \text{if} \quad b_0 = 0 \\ \frac{A_0}{2\sigma_{\text{th}}} \lambda(\boldsymbol{\tau}, \mathbf{b_I}, \tilde{\mathbf{b}}_\mathbf{I}) & \text{if} \quad b_0 = 1 \end{cases} \quad (30)$$

where

$$\lambda'(\boldsymbol{\tau}, \mathbf{b_I}, \tilde{\mathbf{b}}_\mathbf{I}) = 1 - 2\sum_{i=1}^{I} x_i(h(\tau_i, b_i, \tilde{b}_i) - \overline{h})$$

$$\lambda(\boldsymbol{\tau}, \mathbf{b_I}, \tilde{\mathbf{b}}_\mathbf{I}) = 1 + 2\sum_{i=1}^{I} x_i(h(\tau_i, b_i, \tilde{b}_i) - \overline{h}). \quad (31)$$

For $I = 1$, by substituting $u_i^{(b_0)}$ from (16b) and $v^{(b_0)}$ from (30) in (17), the conditional BEP for $b_0 = 0$ and 1 is derived as

$$P_{\mathrm{b}|b_0=0,\boldsymbol{\tau},b_1,\tilde{b}_1} = \frac{1}{2}\text{erfc}\Big(\frac{A_0\,\lambda'(\boldsymbol{\tau}, b_1, \tilde{b}_1)}{2\sqrt{2}\sigma_{\text{th}}}\Big) \quad (32)$$

and (33) at the bottom of this page, respectively. Thus, the exact BEP conditioned to τ_1 is derived as

$$P_{\mathrm{b}|\tau_1}(\gamma, x_1) = \frac{1}{8} \sum_{(b_1,\tilde{b}_1)\in\mathcal{B}} \Big\{ \frac{1}{2}\text{erfc}\Big(\frac{\gamma\,\lambda'(\tau_1, b_1, \tilde{b}_1)}{\sqrt{2}}\Big)$$

$$+ \frac{1}{2}\text{erfc}\Big(\frac{\gamma\,\lambda(\tau_1, b_1, \tilde{b}_1)}{\sqrt{2}}\Big) + \frac{1}{\sqrt{2\pi}} \sum_{k=1}^{\infty} (4\,\gamma^2 x_1 h(\tau_1, b_1, \tilde{b}_1)^2)^k$$

$$\times \frac{1}{(k!)^2} H_{2k-1}(\gamma\,\lambda(\tau_1, b_1, \tilde{b}_1)) \exp\Big(-\frac{(\gamma\,\lambda(\tau_1, b_1, \tilde{b}_1))^2}{2}\Big)\Big\}. \quad (34)$$

In the approximation method, by applying $u_i^{(b_0)}$ from (16b) and $v^{(b_0)}$ from (30) to $F(\mathbf{u}^{(b_0)}, v^{(b_0)})$ in equation (18), the conditional BEP for $b_0 = 0$ is given by (32), and for $b_0 = 1$ is given by (35) at the bottom of this page.

$$P_{\mathrm{b}|b_0=1,\tau_1,b_1,\tilde{b}_1} = \frac{1}{2}\text{erfc}\Big(\frac{A_0\,\lambda(\tau_1, b_1, \tilde{b}_1)}{2\sqrt{2}\sigma_{\text{th}}}\Big) + \frac{1}{\sqrt{2\pi}} \sum_{k=1}^{\infty} \Big(\frac{A_0^2}{\sigma_{\text{th}}^2} x_1 h(\tau_1, b_1, \tilde{b}_1)^2\Big)^k \frac{1}{(k!)^2} H_{2k-1}\Big(\frac{A_0}{2\sigma_{\text{th}}} \lambda(\tau_1, b_1, \tilde{b}_1)\Big)$$

$$\times \exp\Big(-\frac{(A_0^2\,\lambda(\tau_1, b_1, \tilde{b}_1))^2}{8\sigma_{\text{th}}^2}\Big). \quad (33)$$

$$P_{\mathrm{b}|b_0=1,\boldsymbol{\tau},\boldsymbol{b}_\mathbf{I},\tilde{\boldsymbol{b}}_\mathbf{I}} \simeq \frac{1}{2}\text{erfc}\Big(\frac{A_0\,[\lambda(\boldsymbol{\tau}, \boldsymbol{b}_\mathbf{I}, \tilde{\boldsymbol{b}}_\mathbf{I}) - 4\sum_{m=1}^{I} \sqrt{x_m}\,h(\tau_m, b_m, \tilde{b}_m)]}{2\sqrt{2}\,\sigma_{\text{th}}}\Big) \prod_{k=1}^{I} \mathcal{G}\Big(\frac{A_k\,A_0\,h(\tau_k, b_k, \tilde{b}_k)}{2\,\sigma_{\text{th}}^2}$$

$$\times [\lambda(\boldsymbol{\tau}, \boldsymbol{b}_\mathbf{I}, \tilde{\boldsymbol{b}}_\mathbf{I}) - 4\sum_{m=1}^{I} \sqrt{x_m}\,h(\tau_m, b_m, \tilde{b}_m)]\Big). \quad (35)$$

12

By averaging (32) and (35) with respect to $(\boldsymbol{b_I}, \tilde{\boldsymbol{b}}_{\boldsymbol{I}})$, the approximate BEP conditioned to the vector $\boldsymbol{\tau}$ for $I \geq 1$ can be written as

$$
P_{\mathsf{b}|\boldsymbol{\tau}}(\gamma, \mathbf{x}) \simeq \frac{1}{2^{2I+1}} \sum_{(\boldsymbol{b_I}, \tilde{\boldsymbol{b}}_{\mathbf{I}}) \in \mathcal{B}} \frac{1}{2}\mathrm{erfc}\Big(\frac{\gamma\,\lambda'(\boldsymbol{\tau}, \boldsymbol{b_\mathrm{I}}, \tilde{\boldsymbol{b}}_{\mathbf{I}})}{\sqrt{2}}\Big)
$$
$$
+ \frac{1}{2}\mathrm{erfc}\Big(\frac{\gamma}{\sqrt{2}}\big[\lambda(\boldsymbol{\tau}, \boldsymbol{b}_\mathrm{I}, \tilde{\boldsymbol{b}}_\mathbf{I}) - 4\sum_{m=1}^{I}\sqrt{x_m}\,h(\tau_m, b_m, \tilde{b}_m)\big]\Big)
$$
$$
\times \prod_{k=1}^{I}\mathcal{G}(4\,\gamma^2\sqrt{x_k}\,h(\tau_k, b_k, \tilde{b}_k)\,[\lambda(\boldsymbol{\tau}, \boldsymbol{b}_\mathrm{I}, \tilde{\boldsymbol{b}}_\mathbf{I}) - 4\sum_{m=1}^{I}\sqrt{x_m}
$$
$$
\times h(\tau_m, b_m, \tilde{b}_m)]) \, . \tag{36}
$$

APPENDIX B
MIDDLE OF THE EYE (MoE) THRESHOLD

By applying ζ_{moe}, (16a) becomes

$$
v^{(b_0)} = \begin{cases} \frac{A_0}{2\sigma_{\mathrm{th}}}\,\nu'(\boldsymbol{\tau}, \mathbf{b_I}, \tilde{\mathbf{b}}_\mathbf{I}) & \text{if} \quad b_0 = 0 \\ \frac{A_0}{2\sigma_{\mathrm{th}}}\,\nu(\boldsymbol{\tau}, \mathbf{b_I}, \tilde{\mathbf{b}}_\mathbf{I}) & \text{if} \quad b_0 = 1 \end{cases} \tag{37}
$$

where

$$
\nu'(\boldsymbol{\tau}, \mathbf{b_I}, \tilde{\mathbf{b}}_\mathbf{I}) = 1 - 2\sum_{i=1}^{I} x_i\Big(h(\tau_i, b_i, \tilde{b}_i) - 1 + \frac{1}{\sqrt{x_i}}\Big)
$$
$$
\nu(\boldsymbol{\tau}, \mathbf{b_I}, \tilde{\mathbf{b}}_\mathbf{I}) = 1 + 2\sum_{i=1}^{I} x_i\Big(h(\tau_i, b_i, \tilde{b}_i) - 1 + \frac{1}{\sqrt{x_i}}\Big) \, . \tag{38}
$$

Consider (17), where $u_1^{(b_0)}$ and $v^{(b_0)}$ are given by (16b) and (37), respectively. By following the same approach for deriving (34), the exact BEP conditioned to τ_1 $(P_{\mathsf{b}|\tau_1}(\gamma, x_1))$ for $I = 1$ is found to be as

$$
P_{\mathsf{b}|\tau_1}(\gamma, x_1) = \frac{1}{8} \sum_{(b_1, \tilde{b}_1) \in \mathcal{B}} \Big\{ \frac{1}{2}\mathrm{erfc}\Big(\frac{\gamma\,\nu'(\tau_1, b_1, \tilde{b}_1)}{\sqrt{2}}\Big)
$$
$$
+ \frac{1}{2}\mathrm{erfc}\Big(\frac{\gamma\,\nu(\tau_1, b_1, \tilde{b}_1)}{\sqrt{2}}\Big) + \frac{1}{\sqrt{2\pi}}\sum_{k=1}^{\infty}(4\,\gamma^2 x_1 h(\tau_1, b_1, \tilde{b}_1)^2)^k
$$
$$
\times \frac{1}{(k!)^2}\,H_{2k-1}(\gamma\,\nu(\tau_1, b_1, \tilde{b}_1))\,\exp\Big(-\frac{(\gamma\,\nu(\tau_1, b_1, \tilde{b}_1))^2}{2}\Big)\Big\} \, . \tag{39}
$$

For the case with $I \geq 1$, the approximate BEP is obtained following the same steps for deriving (36). Starting from (18), $\mathbf{u}^{(b_0)}$ and $v^{(b_0)}$ are replaced by (16b) and (37), respectively, and finally $P_{\mathsf{b}|\boldsymbol{\tau}}(\gamma, \mathbf{x})$ is derived as

$$
P_{\mathsf{b}|\boldsymbol{\tau}}(\gamma, \mathbf{x}) \simeq \frac{1}{2^{2I+1}} \sum_{(\boldsymbol{b_I}, \tilde{\boldsymbol{b}}_{\mathbf{I}}) \in \mathcal{B}} \frac{1}{2}\mathrm{erfc}\Big(\frac{\gamma\,\nu'(\boldsymbol{\tau}, \boldsymbol{b_\mathrm{I}}, \tilde{\boldsymbol{b}}_{\mathbf{I}})}{\sqrt{2}}\Big)
$$
$$
+ \frac{1}{2}\mathrm{erfc}\Big(\frac{\gamma}{\sqrt{2}}\big[\nu(\boldsymbol{\tau}, \boldsymbol{b}_\mathrm{I}, \tilde{\boldsymbol{b}}_\mathbf{I}) - 4\sum_{m=1}^{I}\sqrt{x_m}\,h(\tau_m, b_m, \tilde{b}_m)\big]\Big)
$$
$$
\times \prod_{k=1}^{I}\mathcal{G}(4\,\gamma^2\sqrt{x_k}\,h(\tau_k, b_k, \tilde{b}_k)[\nu(\boldsymbol{\tau}, \boldsymbol{b}_\mathrm{I}, \tilde{\boldsymbol{b}}_\mathbf{I}) - 4\sum_{m=1}^{I}\sqrt{x_m}
$$
$$
\times h(\tau_m, b_m, \tilde{b}_m)]) \tag{40}
$$

where $\mathcal{G}(\cdot)$ is defined in (19).

APPENDIX C
EXACT BEP EVALUATION FOR $I > 1$

The exact BEP can be evaluated numerically considering the crossed terms in the second sum of equation (4) with $i \neq q$, which is in contrast to the assumption made for deriving (5) and subsequent expressions. Starting from equation (4), the received photocurrent after electrical filtering and sampling becomes

$$
\mathbf{I}^{(n)} = A_0\,b_{0,n} + \sum_{i=1}^{I} A_i\cos(\phi_i)\,b_{0,n}\,h(\tau_i, b_{i,n}, b_{i,n-1}) \tag{41}
$$
$$
+ \sum_{i=1}^{I} B_i\,h(\tau_i, b_{i,n}, b_{i,n-1}) + \sum_{i=1}^{I}\sum_{q=1, q\neq i}^{I}\sqrt{B_i B_q}
$$
$$
\times \cos\,(\phi_i - \phi_q)\,\hat{h}(\tau_i, \tau_q, b_{i,n}, b_{i,n-1}, b_{q,n}, b_{q,n-1})
$$

where

$$
\hat{h}(\tau_i, \tau_q, b_i, \tilde{b}_i, b_q, \tilde{b}_q) = \frac{1}{T_\mathrm{g}}\int_{n\,T}^{n\,T + T_\mathrm{g}} m_i(t)m_q(t)\,dt
$$
$$
= b_i b_q\Big[\frac{T_g - \max(\tau_i, \tau_q)}{T_g}\Big]^{+} + b_i\tilde{b}_q\Big[\frac{T_g - T - \tau_i + \tau_q}{T_g}\Big]^{+}
$$
$$
+ \tilde{b}_i\tilde{b}_q\Big[\frac{T_g - T + \min(\tau_i, \tau_q)}{T_g}\Big]^{+} + \tilde{b}_i b_q\Big[\frac{T_g - T + \tau_i - \tau_q}{T_g}\Big]^{+} \tag{42}
$$

with $[x]^{+} = \max\,(x, 0)$. The expression in (15) for $P_{\mathsf{b}|b_0, \boldsymbol{\tau}, \boldsymbol{b}_\mathrm{I}, \tilde{\boldsymbol{b}}_\mathrm{I}}$ still holds with $u_i^{(b_0)}$ as given by (16b), and

$$
v^{(b_0)} = \begin{cases} [\zeta - \sum_{i=1} B_i h(\tau_i, b_i, \tilde{b}_i) & \text{if} \quad b_0 = 0 \\ - \sum_i \sum_{q\neq i}\sqrt{B_i B_q}\cos\,(\phi_i - \phi_q) \\ \times \hat{h}(\tau_i, \tau_q, b_i, \tilde{b}_i, b_q, \tilde{b}_q)]/\sigma_{\mathrm{th}} \\ \\ [-\zeta + A_0 + \sum_i B_i\,h(\tau_i, b_i, \tilde{b}_i) & \text{if} \quad b_0 = 1 \\ + \sum_i \sum_{q\neq i}\sqrt{B_i B_q}\cos\,(\phi_i - \phi_q) \\ \times \hat{h}(\tau_i, \tau_q, b_i, \tilde{b}_i, b_q, \tilde{b}_q)]/\sigma_{\mathrm{th}} \, . \end{cases} \tag{43}
$$

Then, $P_{\mathsf{b}|\boldsymbol{\tau}}(\gamma, \mathbf{x})$ is given by substituting $P_{\mathsf{b}|b_0, \boldsymbol{\tau}, \boldsymbol{b}_\mathrm{I}, \tilde{\boldsymbol{b}}_\mathrm{I}}$ in (12) and (13), and finally is averaged by (24). The decision threshold for the AOP case does not change in (20), but for the MoE threshold, the expression in (22) slightly changes. However, the results for the exact BEP in Section V are provided with the same thresholds as defined in Section IV, in order to compare the exact BEP with the approximate one.

REFERENCES

[1] H. Elgala, R. Mesleh, and H. Haas, "Indoor optical wireless communication: potential and state-of-the-art," *IEEE Commun. Mag.*, vol. 49, no. 9, pp. 56–62, Sep. 2011.

[2] M. A. Khalighi and M. Uysal, "Survey on free space optical communication: A communication theory perspective," *IEEE Commun. Surveys Tuts.*, vol. 16, no. 4, pp. 2231–2258, Jun. 2014.

[3] M. Z. Chowdhury, M. T. Hossan, A. Islam, and Y. M. Jang, "A comparative survey of optical wireless technologies: Architectures and applications," *IEEE Access*, vol. 6, pp. 9819–9840, Jan. 2018.

[4] M. Nafari, L. Feng, and J. Jornet, "On-chip wireless optical channel modeling for massive multi-core computing architectures," in *Proc. IEEE Wireless Commun. and Networking Conf.*, San Francisco, CA, USA, Mar. 2017, pp. 1–6.

This article has been accepted for publication in a future issue of this journal, but has not been fully edited. Content may change prior to final publication. Citation information: DOI 10.1109/TCOMM.2019.2960339, IEEE Transactions on Communications

13

[5] G. Bellanca, G. Calo, A. E. Kaplan, P. Bassi, and V. Petruzzelli, "Integrated Vivaldi plasmonic antenna for wireless on-chip optical communications," *Optics Express*, vol. 25, no. 14, pp. 16 214–16 227, Jun. 2017.

[6] F. Fuschini, M. Barbiroli, M. Zoli, G. Bellanca, G. Calò, P. Bassi, and V. Petruzzelli, "Ray tracing modeling of electromagnetic propagation for on-chip wireless optical communications," *J. Low Power Electron. Appl.*, vol. 8, no. 4, Oct. 2018.

[7] L. Benini and G. D. Micheli, "Networks on chips: a new SoC paradigm," *IEEE Computer*, vol. 35, no. 1, pp. 70–78, Jan. 2002.

[8] P. P. Pande, C. Grecu, M. Jones, A. Ivanov, and R. Saleh, "Performance evaluation and design trade-offs for network-on-chip interconnect architectures," *IEEE Trans. Comput.*, vol. 54, no. 8, pp. 1025–1040, Aug. 2005.

[9] J. D. Owens, W. J. Dally, R. Ho, D. N. Jayasimha, S. W. Keckler, and L.-S. Peh, "Research challenges for on-chip interconnection networks," *IEEE Micro*, vol. 27, no. 5, pp. 96–108, Nov. 2007.

[10] J. Kim, K. Choi, and G. Loh, "Exploiting new interconnect technologies in on-chip communication," *IEEE J. Emerg. Select. Top. Circuits Syst.*, vol. 2, no. 2, pp. 124–136, Jun. 2012.

[11] A. Biberman and K. Bergman, "Optical interconnection networks for high-performance computing systems," *Reports on Progress in Physics*, vol. 75, no. 4, Apr. 2012.

[12] A. Karkar, T. Mak, K.-F. Tong, and A. Yakovlev, "A survey of emerging interconnects for on-chip efficient multicast and broadcast in many-cores," *IEEE Circuits Syst. Mag.*, vol. 16, no. 1, pp. 58–72, Feb. 2016.

[13] S. Werner, J. Navaridas, and M. Luján, "A survey on optical network-on-chip architectures," *ACM Comput. Surv.*, vol. 50, no. 6, pp. 3682–3695, Jan. 2018.

[14] S. Deb, K. Chang, X. Yu, S. P. Sah, M. Cosic, A. Ganguly, P. P. Pande, B. Belzer, and D. Heo, "Design of an energy-efficient CMOS-compatible NoC architecture with millimeter-wave wireless interconnects," *IEEE Trans. Comput.*, vol. 62, no. 12, pp. 2382–2396, Dec. 2013.

[15] X. Yu, J. Baylon, P. Wettin, D. Heo, P. P. Pande, and S. Mirabbasi, "Architecture and design of multichannel millimeter-wave wireless NoC," *IEEE Des. Test*, vol. 31, no. 6, pp. 19–28, Dec. 2014.

[16] M. A. I. Sikder, A. K. Kodi, M. Kennedy, S. Kaya, and A. Louri, "OWN: Optical and wireless network-on-chip for kilo-core architectures," in *IEEE 23rd Annu. Symp. High-Perform. Interconnects*, Santa Clara, CA, USA, Aug. 2015, pp. 44–51.

[17] D. DiTomaso, A. Kodi, D. Matolak, S. Kaya, S. Laha, and W. Rayess, "A-WiNoC: Adaptive wireless network-on-chip architecture for chip multiprocessors," *IEEE Trans. Parallel Distrib. Syst.*, vol. 26, no. 12, pp. 3289–3302, Dec. 2015.

[18] M. O. Agyeman, Q. T. Vien, A. Ahmadnia, A. Yakovlev, K. F. Tong, and T. Mak, "A resilient 2-D waveguide communication fabric for hybrid wired-wireless NoC design," *IEEE Trans. Parallel Distrib. Syst.*, vol. 28, no. 2, pp. 359–373, Feb. 2017.

[19] A. Ganguly, K. Chang, S. Deb, P. P. Pande, B. Belzer, and C. Teuscher, "Scalable hybrid wireless network-on-chip architectures for multicore systems," *IEEE Trans. Comput.*, vol. 60, no. 10, pp. 1485–1502, Oct. 2011.

[20] S. Abadal, A. Mestres, J. Torrellas, E. Alarcon, and A. Cabellos-Aparicio, "Medium access control in wireless network-on-chip: A context analysis," *IEEE Commun. Mag.*, vol. 56, no. 6, pp. 172–178, Jun. 2018.

[21] A. Shacham, K. Bergman, and L. P. Carloni, "Photonic networks-on-chip for future generations of chip multiprocessors," *IEEE Trans. Comput.*, vol. 57, no. 9, pp. 1246–1260, Sep. 2008.

[22] M. Haurylau, G. Chen, H. Chen, J. Zhang, N. Nelson, D. H. Albonesi, E. G. Friedman, and P. M. Fauchet, "On-chip optical interconnect roadmap: Challenges and critical directions," *IEEE J. Sel. Topics Quantum Electron.*, vol. 12, no. 6, pp. 1699–1705, Dec. 2006.

[23] D. W. Matolak, A. Kodi, S. Kaya, D. Ditomaso, S. Laha, and W. Rayess, "Wireless networks-on-chips: architecture, wireless channel, and devices," *IEEE Wireless Commun.*, vol. 19, no. 5, pp. 1536–1284, Oct. 2012.

[24] S. Abadal, M. Iannazzo, M. Nemirovsky, A. Cabellos-Aparicio, H. Lee, and E. Alarcón, "On the area and energy scalability of wireless network-on-chip: A model-based benchmarked design space exploration," *IEEE/ACM Trans. Netw.*, vol. 23, no. 5, pp. 1501–1513, Oct. 2015.

[25] S. Deb, A. Ganguly, P. P. Pande, B. Belzer, and D. Heo, "Wireless NoC as interconnection backbone for multicore chips: Promises and challenges," *IEEE J. Emerg. Sel. Topics Circuits. Syst.*, vol. 2, no. 2, pp. 228–239, Jun. 2012.

[26] H. Zhou, Z. Li, L. Shang, A. Mickelson, and D. S. Filipovic, "On-chip wireless optical broadcast interconnection network," *J. Lightw. Technol.*, vol. 28, no. 24, pp. 3569–3577, Dec. 2010.

[27] S. Abadal, A. Mestres, M. Nemirovsky, H. Lee, A. Gonzàlez, E. Alarcòn, and A. Cabellos-Aparicio, "Scalability of broadcast performance in wireless network-on-chip," *IEEE Trans. Parallel Distrib. Syst.*, vol. 27, no. 12, pp. 3631–3645, Dec. 2016.

[28] A. Karkar, T. Mak, N. Dahir, R. Al-Dujaily, K.-F. Tong, and A. Yakovlev, "Network-on-chip multicast architectures using hybrid wire and surface-wave interconnects," *IEEE Trans. Emerg. Topics Comput.*, vol. 6, no. 3, pp. 357–369, Apr. 2018.

[29] H. K. Mondal, S. H. Gade, M. S. Shamim, S. Deb, and A. Ganguly, "Interference-aware wireless network-on-chip architecture using directional antennas," *IEEE Trans. Multi-Scale Comput. Syst.*, vol. 3, no. 3, pp. 193–205, Jul. 2017.

[30] S. Abadal, J. Torrellas, E. Alarcón, and A. Cabellos-Aparicio, "OrthoNoC: A broadcast-oriented dual-plane wireless network-on-chip architecture," *IEEE Trans. Parallel Distrib. Syst.*, vol. 29, no. 3, pp. 628–641, Mar. 2018.

[31] D. W. Matolak, S. Kaya, and A. Kodi, "Channel modeling for wireless networks-on-chips," *IEEE Commun. Mag.*, vol. 51, no. 6, pp. 180–186, Jun. 2013.

[32] E. L. Goldstein, L. Eskildsen, and A. F. Elrefaie, "Performance implications of component crosstalk in transparent lightwave networks," *IEEE Photon. Technol. Lett.*, vol. 6, no. 5, pp. 657–660, May 1994.

[33] K.-P. Ho, C.-K. Chan, F. Tong, and L. K. Chen, "Exact analysis of homodyne crosstalk induced penalty in WDM networks," *IEEE Photon. Technol. Lett.*, vol. 10, no. 3, pp. 457–458, Mar. 1998.

[34] K.-P. Ho, "Analysis of homodyne crosstalk in optical networks using Gram-Charlier series," *J. Lightw. Technol.*, vol. 17, no. 2, pp. 149–154, Feb. 1999.

[35] E. Iannone, R. Sabella, M. Avattaneo, and G. de Paolis, "Modeling of in-band crosstalk in WDM optical networks," *J. Lightw. Technol.*, vol. 17, no. 7, pp. 1135–1141, Jul. 1999.

[36] T. Kamalakis, T. Sphicopoulos, and M. Sagriotis, "Accurate estimation of the error probability in the presence of in-band crosstalk noise in WDM networks," *J. Lightw. Technol.*, vol. 21, no. 10, pp. 2172–2181, Oct. 2003.

[37] S. D. Dods and T. B. Anderson, "Calculation of bit-error rates and power penalties due to incoherent crosstalk in optical networks using Taylor series expansions," *J. Lightw. Technol.*, vol. 23, no. 4, pp. 1828–1837, Apr. 2005.

[38] S. Sarkar and N. R. Das, "Study of component crosstalk and obtaining optimum detection threshold for minimum bit-error-rate in a WDM receiver," *J. Lightw. Technol.*, vol. 27, no. 19, pp. 4366–4373, Oct. 2009.

[39] G. W. Marsh and J. M. Kahn, "Channel reuse strategies for indoor infrared wireless communications," *IEEE Trans. Commun.*, vol. 45, no. 10, pp. 1280–1290, Oct. 1997.

[40] K.-P. Ho, "Analysis of co-channel crosstalk interference in optical networks," *Electron. Lett.*, vol. 34, no. 4, pp. 383–385, Feb. 1998.

[41] F. Zafar, M. Bakaul, and R. Parthiban, "Laser-diode-based visible light communication: toward Gigabit class communication," *IEEE Commun. Mag.*, vol. 55, no. 2, pp. 144–151, Feb. 2017.

[42] M. I. Hayee and A. E. Willner, "NRZ versus RZ in 10-40-Gb/s dispersion-managed WDM transmission systems," *IEEE Photon. Technol. Lett.*, vol. 11, no. 8, pp. 991–993, Aug. 1999.

[43] G. P. Agrawal, *Lightwave Technology: Telecommunication Systems*. Hoboken, NJ: Published by John Wiley & Sons, Inc., 2005.

[44] J. Shafiei Dehkordi, V. Tralli, M. Barbiroli, J. Nanni, F. Fuschini, and V. Petruzzelli, "Analysis, design and performance evaluation of on-chip optical wireless links," in *ICQNM*, Nice, France, Oct. 2019, pp. 1–6.

Jinous Shafiei Dehkordi received the Laurea (*summa cum laude*) degree in computer and automation engineering in 2012 from the University of Ferrara, Ferrara, Italy, where she obtained the Ph.D. degree (*cum laude*) in Telecommunication Engineering in 2017. Since 2013, she is a Research Collaborator with Wireless Communication Laboratory at the Department of Engineering, University of Ferrara. Her current research interests include adaptive diversity communications, interference characterization, stochastic wireless networks, statistical signal processing, radio localization techniques, and optical wireless communications in network-on-chips. She served as a TPC member for IEEE conferences and as a reviewer for IEEE journals.

Velio Tralli (M'94-SM'05) received the Dr. Ing. degree in electronic engineering (cum laude) and the Ph.D. degree in electronic engineering and computer science from the University of Bologna, Bologna, Italy, in 1989 and 1993, respectively.

From 1994 to 1999, he was a Researcher with the National Research Council at CSITE, University of Bologna. In 1999, he joined the Department of Engineering, University of Ferrara, Ferrara, Italy, where he is currently an Associate Professor. He authored or coauthored more than one hundred papers in refereed journals, including transactions of the IEEE, and international conferences. He participated in several national and European research projects addressing short-range communications systems, wireless sensor networks, 3G-4G wireless networks, and wireless video communications. His research interests include digital transmission and coding, and wireless communications, with emphasis on radio resource optimization, cross-layer design, multicarrier and multiantenna systems. He is a Senior Member of IEEE, where he serves as a Reviewer for journals/transactions, and as a TPC Member for several international conferences. He is an Associate Editor for the European Transactions on Emerging Technologies. He also served as a Co-Chair for the Wireless Communication Symposium of ICC 2006 and for the Communication Theory Symposium of ICC 2013.